RSC Advances

PAPER

View Article Online
View Journal | View Issue

Cite this: *RSC Adv.*, 2017, **7**, 42997

Construction of full-spectrum-driven Ag–g-C_3N_4/$W_{18}O_{49}$ heterojunction catalyst with outstanding N_2 photofixation ability

Hongyu Liang, Jianzhong Li* and Yanwen Tian*

More than half of the solar spectrum is near infrared (NIR) light, which is seldom utilized in photocatalytic reactions. In this work, an Ag–g-C_3N_4/$W_{18}O_{49}$ heterojunction catalyst is prepared and used for full-spectrum-driven N_2 photofixation from the UV to the NIR region for the first time. X-ray diffraction, N_2 adsorption, UV-Vis-NIR spectroscopy, thermogravimetric analysis, photoluminescence, X-ray photoelectron spectroscopy and electrochemical impedance spectra were used to characterize the prepared catalysts. The result indicates that the as-prepared Ag–g-C_3N_4/$W_{18}O_{49}$ heterojunction catalysts display much higher N_2 photofixation performance than that of individual $W_{18}O_{49}$ or Ag–g-C_3N_4, which should be due to the better separation rate of electron–hole pairs and more efficient light utilization. g-C_3N_4 is the active component in the catalyst for N_2 photofixation. Ag loading promotes the separation rate of electron–hole pairs. $W_{18}O_{49}$ plays a role as light absorber in the full-spectrum to form more photogenerated electrons for recombining the holes in the g-C_3N_4 through "Z-scheme" mechanism. A possible electrons transfer route is proposed.

Received 31st July 2017
Accepted 29th August 2017

DOI: 10.1039/c7ra08420j

rsc.li/rsc-advances

Introduction

Energy issues are one of the problems that need to be solved in today's world. With the increasing demands of environmental regulations, traditional fossil fuels are being gradually replaced by new clean energy sources such as wind, solar, nuclear, *etc.* By using sunlight to drive a series of important chemical reactions, semiconductor photocatalytic oxidation technology can convert low-density solar energy into high-density chemical energy or mineralize organic pollutants directly. So this technology shows great potential in addressing energy shortages and environmental pollution.[1–4] According to the solar spectrum, sunlight is composed of 5% ultraviolet (below 400 nm), 43% visible light (400–750 nm), and 52% near infrared (NIR, above 750 nm).[5] Despite that great efforts have been made to broaden the photoresponsive region of photocatalysts to utilize as much solar energy as possible, near infrared light has seldom been utilized in previous work.[6–12]

Nitrogen is a necessary element for the growth of plants and animals. Therefore, nitrogen fixation is the most important chemical reaction in nature after photosynthesis. At present, the use of the Haber method as an industrial nitrogen fixation process has reached an annual level of 100 million tons. This method requires high temperature and pressure as well as the presence of hydrogen. Not only are the raw material costs and energy consumption high for this process, there is a certain risk. In 1977, Schrauzer *et al.* for the first time found that Fe-doped TiO_2 powder can photocatalytically reduce nitrogen to form ammonia.[13] The standard redox potential for N_2/NH_3 = −0.0922 V against NHE. Since then, many photocatalysts, such as precious metals supported on TiO_2, $Fe_2Ti_2O_7$, graphite-phase carbon nitride, bismuth oxyhalide and polymetallic sulfide, have been reported successively.[14–18] However, because the photocatalytic nitrogen fixation is not a thermodynamically spontaneous reaction, the N_2 photofixation abilities of these catalysts are not satisfactory.

Recently, graphitic carbon nitride (g-C_3N_4) has attracted a great deal of interest in photocatalytic applications. The heptazine ring structure and high condensation degree grant it many advantages, such as good chemical stability, an appropriate band gap energy and a unique electronic structure. All of these render g-C_3N_4 the best candidate for photocatalytic applications such as pollutant degradation,[19] water reduction and oxidation[20] CO_2 capture,[21] N_2 photofixation[22] and organic synthesis.[23] However, the shortcomings of g-C_3N_4 are as obvious as its advantages, including a low visible light utilization efficiency and rapid recombination of the photogenerated electron–hole pairs. Noble metal loading, such as Pt, Pd, Rh, Ru and Ag, is a effective method to promote the electron–hole separation rate. Ag, as a relatively inexpensive noble metal cocatalyst, plays a good role in promoting the photoelectron migration, which has been widely used in photocatalytic H_2 production, CO_2 and heavy metal reduction.[24–26] Not only that, it has been reported that noble metal (Pt, Pd, Rh, Ru) modification could promote the photocatalytic N_2 fixation ability of TiO_2 catalyst.

School of Metallurgy, Northeastern University, Shenyang 110819, China. E-mail: lijianzhongnu@163.com

The results show that the NH_4^+ yield is related to the strength of the metal–hydrogen bond. However, to the best of our knowledge, no literature concerning Ag loaded photocatalyst for nitrogen fixation is reported. Building heterojunction, as one of the solutions, has also been widely investigated.[27–34] The photogenerated electrons of a component across the heterojunction to recombine with the holes generated in another component. The remaining electrons and holes will be located on two different components, thus the separation rate is promoted. However, it is not easy for electrons to across the heterojunction because of the poor interaction between two components, leading to that the separation efficiency is not as good as expected. Thus it is imagined that if the heterojunction catalyst can have higher light absorption ability, more photoelectrons will be excited to across the heterojunction.

Monoclinic $W_{18}O_{49}$, as the only oxide isolated in a single phase, has been extensively studied as photocatalyst in recent years.[6,35–37] $W_{18}O_{49}$ has a suitable band gap energy, as well as a large number of oxygen vacancies, which can provide active sites for reaction substrate.[38,39] Not only that, because of the presence of mixed-valence W ions, $W_{18}O_{49}$ shows strong absorption in near infrared light.[40] Thus, it is imagined that coupling $W_{18}O_{49}$ with other semiconductor to construct heterojunction catalyst can not only improve the solar utilization, especially in near infrared region, but depress recombination of the photogenerated electron–hole pairs. Guo *et al.* prepared $W_{18}O_{49}$ sensitized TiO_2 spheres with full-spectrum-driven photocatalytic dye degradation activities from UV to near infrared.[6] The as-prepared heterojunction catalyst displayed strong optical absorption in the whole region of 300–2500 nm, thus shows desired photocatalytic properties for the full utilization of all solar energy. W^{5+} site in $W_{18}O_{49}$ played important role on photocatalytic performance. Chang *et al.* prepared Ag/AgCl/$W_{18}O_{49}$ nanorods heterostructures.[12] The promoted photocatalytic antibacterial activity can be attributed to both the surface plasmon resonance of noble metal and the synergistic effect of plasmonic photocatalyst and oxide semiconductor photocatalyst. In this work, Ag–g-C_3N_4/$W_{18}O_{49}$ heterojunction catalyst is prepared and used for full-spectrum-driven N_2 photofixation from UV to NIR region for the first time. The effect of NIR light on the N_2 photofixation ability over as-prepared catalysts is investigated by using combined light source. The as-prepared composite shows much higher NH_4^+ generation rate than that of single $W_{18}O_{49}$ or Ag–g-C_3N_4. The effect of NIR light on the N_2 photofixation ability over as-prepared heterojunction catalyst is investigated. The possible reaction mechanism and electrons transfer route are proposed.

Experimental

Preparation and characterization

$W_{18}O_{49}$ was prepared as follow. A certain amount of WCl_6 was dissolved in 50 mL of ethanol to form a 15 mM solution. This solution was transferred into a Teflon-lined autoclave and heated at 200 °C for 24 h. The obtained solid was collected by centrifugation and washed repeatedly with water and ethanol, followed by drying at 80 °C. Neat g-C_3N_4 was prepared by heating melamine at 550 °C for 4 h at the rate of 5 °C min^{-1} under Ar atmosphere and denoted as gCN. 1 g of gCN was dispersed into 50 mL of water under stirring and ultrasonicated for 2 h. $AgNO_3$ was added into above suspension. Then, a certain amount of sodium borohydride was added (molar ratio $AgNO_3$/sodium borohydride = 1 : 5) and stirred for 2 h. The product was washed by water and ethanol for several times, dried at 60 °C and denoted as Ag(x%)–gCN, where x% stands for the mass percentage of Ag.

For Ag–g-C_3N_4/$W_{18}O_{49}$ composite, Ag(1%)–gCN and $W_{18}O_{49}$ (mass ratio = 4 : 1, 2 : 1, 1 : 1 and 1 : 2) were dispersed into 50 mL of ethanol under stirring and ultrasonicated for 2 h. After evaporating ethanol under low temperature, the obtained mixture was annealed at 500 °C for 2 h at the rate of 5 °C min^{-1} under Ar atmosphere. The obtained product was denoted as Ag(1%)–gCN/$W_{18}O_{49}$(4 : 1), Ag(1%)–gCN/$W_{18}O_{49}$(2 : 1), Ag(1%)–gCN/$W_{18}O_{49}$(1 : 1) and Ag(1%)–gCN/$W_{18}O_{49}$(1 : 2), respectively. In order to investigate the effect of NIR light on the photocatalytic N_2 fixation ability of as-prepared heterojunction catalysts, $W_{18}O_{49}$ was annealed at 500 °C for 2 h in air to form WO_3. Then WO_3 was used to prepare the composite following the same procedure. The product was denoted as Ag(1%)–gCN/WO_3(1 : 1).

The XRD patterns were registered on a Rigaku D/max-2400 instrument using Cu-K_α radiation (λ = 1.54 Å). The optical properties were measured using a spectrophotometer (CARY5000), giving an output of transmittance from UV to NIR region. Thermogravimetric analysis (TG) was performed using a TGA-DSC 2 (Mettler-Toledo) instrument. Nitrogen adsorption was measured at −196 °C on a Micromeritics 2010 analyser. The BET surface area (S_{BET}) was calculated based on the adsorption isotherm. The XPS measurements were carried out on a Thermo Escalab 250 XPS system with Al K_α radiation as the excitation source. The photoluminescence (PL) spectra were measured at room temperature with a fluorospectrophotometer (FP-6300) using a Xe lamp as the excitation source. Electrochemical impedance spectra (EIS) was registered *via* an EIS spectrometer (EC-Lab SP-150, BioLogic Science Instruments) in a three-electrode cell by applying 10 mV alternative signal *versus* the reference electrode (SCE) over the frequency range of 1 MHz to 100 mHz. The photocurrents were measured using an electrochemical analyzer (CHI 618C Instruments) equipped with a rectangular-shaped quartz reactor (20 × 40 × 50 mm) using a standard three-electrode system. The prepared sample film was used as the working electrode, a Pt flake was used as the counter electrode, and Ag/AgCl was used as the reference electrode. A 500 W Xe lamp was used to irradiate the working electrode from the back side. The light intensity on the working electrode was 120 mW cm^{-2}.

Photocatalytic reaction

The nitrogen photofixation performance of prepared catalysts was evaluated according to previous work.[41] The experiments were performed in a double-walled quartz reactor using 300 W Xe lamp and 200 W infrared light together as a simulated solar light source. Light of λ > 800 nm and λ < 800 nm was removed by

optical filters for Xe lamp and infrared light, respectively. 0.2 g of catalyst was added to a 500 mL deionized water. Ethanol (0.789 g L^{-1}) was added as a hole scavenger. The suspension was dispersed using an ultrasonicator for 10 min. 5 mL of the suspension were collected at given time intervals, and immediately centrifuged to separate the liquid samples from the solid catalyst. The concentration of NH_4^+ was measured using the Nessler's reagent spectrophotometry method (JB7478-87) with a UV-2450 spectrophotometer (Shimadzu, Japan).[17,41]

Results and discussion

XRD patterns of as-prepared catalysts are shown in Fig. 1. $W_{18}O_{49}$ displays mainly two diffraction peaks, corresponding to the (0 1 0) and (2 1 0) crystal faces of the monoclinic $W_{18}O_{49}$ structure.[42] For gCN, two diffraction peaks locate at 13.1° and 27.5°, which are assigned to the (1 0 0) and (0 0 2) crystal planes.[43] For Ag(1%)–gCN, no Ag diffraction peak is observed, which is probably due to the low content and high dispersion. As expected, all XRD diffraction peaks of as-prepared heterojunction catalysts reveal a coexistence of $W_{18}O_{49}$ and gCN. Furthermore, the peak intensity of $W_{18}O_{49}$ increases with increasing $W_{18}O_{49}$ content.

The optical property is a critical factor to influence the photocatalytic performance of materials. The powder absorbance spectra of as-prepared catalysts were given in Fig. 2a. gCN shows the typical absorption curve of semiconductor with the absorption edge of 460 nm. Ag(1%)–gCN shows the low visible light absorption because of the surface plasmon effect.[44] For $W_{18}O_{49}$, it can be clearly seen that the blue sample exhibits strong optical absorption in the whole solar region of 250–1800 nm, especially for the NIR region from 750 to 1800 nm. Benefitting from the addition of $W_{18}O_{49}$, the as-prepared heterojunction catalysts display enhanced absorption in the whole solar region, accompanying with the color change from cambridge blue for Ag(1%)–gCN/$W_{18}O_{49}$(4 : 1) to dark blue for Ag(1%)–gCN/$W_{18}O_{49}$(1 : 2). The TG analysis is shown in Fig. 2b. For gCN, the beginning temperature of the weight loss is approximately at 600 °C. The weight loss is 100% when the temperature rises to 750 °C, which is mainly attributed to the sublimation or decomposition of g-C_3N_4. For Ag(1%)–gCN/$W_{18}O_{49}$(1 : 1), the similar weight loss curve is obtained, whereas 53 wt% sample is remained. This remains should be WO_3. The $W_{18}O_{49}$ content for Ag(1%)–gCN/$W_{18}O_{49}$(4 : 1), Ag(1%)–gCN/$W_{18}O_{49}$(2 : 1), Ag(1%)–gCN/$W_{18}O_{49}$(1 : 1) and Ag(1%)–gCN/$W_{18}O_{49}$(1 : 2) measured by TG analysis is 21 wt%, 34.5 wt%, 53 wt% and 67.4 wt%, respectively.

XPS is used to investigate the state of the elements on the catalyst surface (Fig. 3). In C 1s region, the peak with binding energy of 284.6 eV is assigned to the graphitic species in the CN matrix. The peak located at 287.9 eV should be attributed to the sp^2 hybridized carbon atoms bonded to aliphatic amine.[45,46] In N 1s region (Fig. 3b), the main peak located at 398.2 eV is attributed to sp^2 hybridized nitrogen (C=N–C), confirming the structure of graphitic carbon nitride. The peak with binding energy of 400.4 eV is assigned to tertiary nitrogen (N–$(C)_3$) groups.[47] In Ag 3d region (Fig. 3c), two peaks located at 368.2 and 374.2 eV are assigned to the metallic Ag.[48] For W 4f region (Fig. 3d), the spectra of $W_{18}O_{49}$ and Ag(1%)–gCN/$W_{18}O_{49}$(1 : 1) can be fitted with four contributions. Two peaks at 35.6 and 37.6 eV is attributed to W^{6+}, and the other two peaks at 34.7 and 36.8 eV is assigned to W^{5+} or W^{4+}.[42,49] This result confirms the

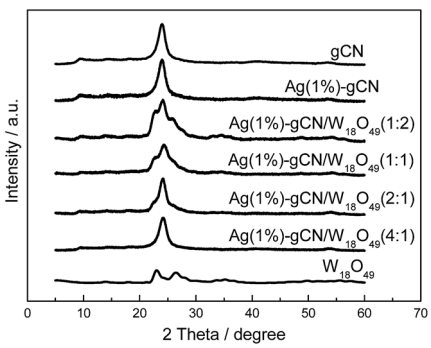

Fig. 1 XRD patterns of as-prepared catalysts.

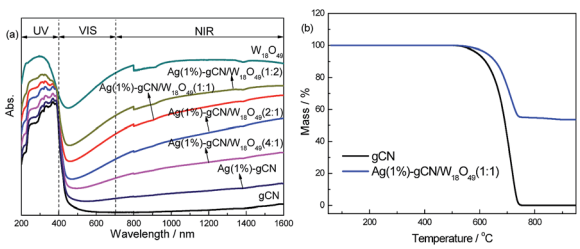

Fig. 2 Powder absorbance spectra of as-prepared samples from UV to near infrared region (a) and TG analysis (b).

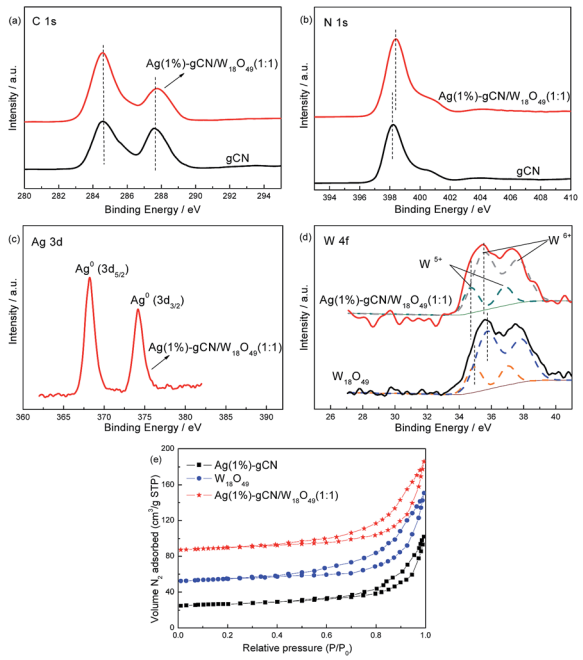

Fig. 3 XPS spectra (a–d) and N_2 adsorption (e) of gCN, $W_{18}O_{49}$ and Ag(1%)–gCN/$W_{18}O_{49}$(1 : 1).

as-prepared catalyst is $W_{18}O_{49}$ but not WO_3. In addition, no difference between gCN and Ag(1%)–gCN/$W_{18}O_{49}$(1 : 1) can be observed in C 1s region. However, in the regions of N 1s and W 4f, ~0.2 eV shifts are obviously shown. This hints the strong interaction between $W_{18}O_{49}$ and gCN exist. To characterize the specific surface area of as-prepared catalysts, the nitrogen adsorption and desorption isotherms were measured (Fig. 3e). The isotherms of all the samples are of classical type IV, suggesting the presence of mesopores. The BET specific surface areas (S_{BET}) of gCN, Ag(1%)–gCN, $W_{18}O_{49}$, Ag(1%)–gCN/$W_{18}O_{49}$(4 : 1), Ag(1%)–gCN/$W_{18}O_{49}$(2 : 1), Ag(1%)–gCN/$W_{18}O_{49}$(1 : 1) and Ag(1%)–gCN/$W_{18}O_{49}$(1 : 2) are calculated to be 8.2, 8.3, 8.7, 8.8, 8.9, 8.5 and 8.4 $m^2 g^{-1}$. This indicates the as-prepared catalysts show the comparable S_{BET}.

Fig. 4 shows the morphology of as-prepared catalysts. It can be seen that the gCN shows the layered structure, similar to the analogue graphite (Fig. 4a). The morphology of $W_{18}O_{49}$ is nanorods, with the size of 2 μm length × 0.4 μm width (Fig. 4b). Fig. 4c shows that Ag(1%)–gCN/$W_{18}O_{49}$(1 : 1) display two obvious different morphologies. The layered structure should be g-C_3N_4. These nanorods, which attached on the g-C_3N_4 surface, should be $W_{18}O_{49}$. The TEM image of Ag(1%)–gCN/$W_{18}O_{49}$(1 : 1) displays that the Ag nanoparticles, with the size of 5 nm, are uniformly dispersed on the catalyst surface (Fig. 4d).

The effective separation of photogenerated electron–hole pairs can provide sufficient photoelectrons to reduce the N_2 molecules. Fig. 5a shows the EIS spectra of as-prepared catalysts. $W_{18}O_{49}$ and gCN exhibit larger arc radius than other catalysts, suggesting a larger resistance of working electrodes, which is harmful to the charge transmission.[50] Ag(1%)–gCN shows smaller arc radius than gCN, due to the promoted separation rate by Ag loading. For the as-prepared heterojunction catalysts, the arc radius are obviously reduced, indicating that more effective separation of photogenerated electron–hole pairs occurs. Ag(1%)–gCN/$W_{18}O_{49}$(1 : 1) displays

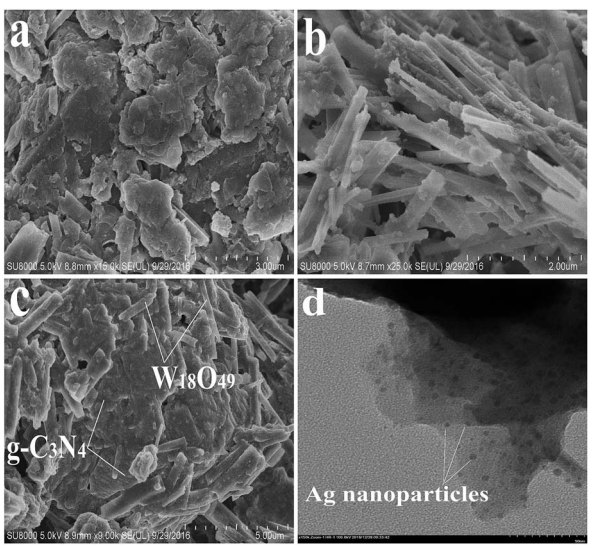

Fig. 4 SEM images of gCN (a), $W_{18}O_{49}$ (b), Ag(1%)–gCN/$W_{18}O_{49}$(1 : 1) (c) and TEM image of Ag(1%)–gCN/$W_{18}O_{49}$(1 : 1) (d).

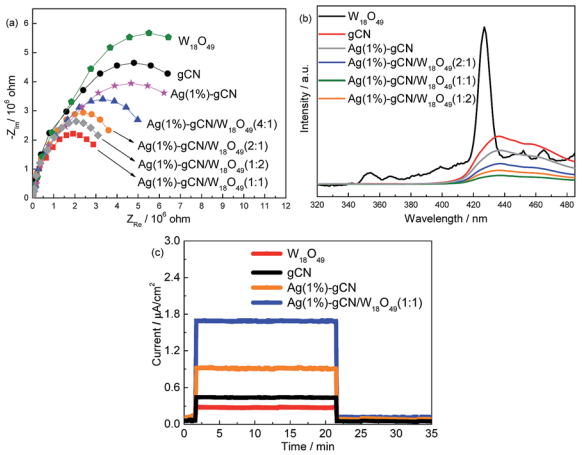

Fig. 5 EIS (a), PL (b) and photocurrent (c) of as-prepared catalysts.

the most effective separation rate among the catalysts. Fig. 5b shows the PL spectra of as-prepared catalysts using excitation at 255 nm. $W_{18}O_{49}$ exhibits a emission peak centered at 430 nm, which was attributed to the intrinsic band to band transition emission. The week emissions around 350, 450 and 465 nm should be assigned to the defects such as oxygen vacancies.[51] For gCN, broad PL band around 450 nm is observed with the energy of light approximately equal to the band gap of gCN. Such band–band PL signal is attributed to excitonic PL, which mainly results from the n–π* electronic transitions involving lone pairs of nitrogen atoms in g-C_3N_4.[52] In the case of as-prepared heterojunction catalysts, the PL spectra show the similar shape to that of gCN, whereas the intensities are obviously decreased. Ag(1%)–gCN/$W_{18}O_{49}$(1 : 1) shows the lowest PL intensity, hinting its most effective separation rate of electrons and holes. This is consistent with the EIS results. The photocurrent densities of as-prepared catalysts are also measured. As shown in Fig. 5c, neat gCN and $W_{18}O_{49}$ show the low photocurrent densities. After loading with Ag, the photocurrent density of Ag(1%)–gCN obviously improves. In the case of Ag(1%)–gCN/$W_{18}O_{49}$(1 : 1), the photocurrent density further improves because of the formation of heterojunction.

The influence of Ag content on nitrogen photofixation performance is presented in Table 1. The result shows that, without Ag loading, the NH_4^+ generation rate ($r(NH_4^+)$) for gCN is only 0.36 mg L^{-1} h^{-1} g_{cat}^{-1}. Ag(1%)–gCN display the highest $r(NH_4^+)$, 0.57 mg L^{-1} h^{-1} g_{cat}^{-1}. Further increasing the Ag content causes the decreased $r(NH_4^+)$ for Ag(2%)–gCN. This decreased photocatalytic activity results not only from an increased electrons–holes recombination but also from the trivial light shielding effect by strongly absorbing of Ag. Thus the optimal loading amount for Ag is 1 wt%.

Table 1 The influence of Ag content on nitrogen photofixation performance

Ag content	0	0.5 wt%	1 wt%	2 wt%
$r(NH_4^+)$/mg L^{-1} h^{-1} g_{cat}^{-1}	0.36	0.48	0.57	0.39

Fig. 6a displays the N_2 photofixation ability over as-prepared catalysts. The control experiment indicates that the NH_4^+ concentrations are very low (<0.01 mg L^{-1} h^{-1} g_{cat}^{-1}) in the absence of photocatalyst, N_2 or light irradiation. This hints that NH_4^+ is formed *via* a photocatalytic process. The $r(NH_4^+)$ of neat $W_{18}O_{49}$ can be ignorant, hinting the active component in the heterojunction catalyst is not $W_{18}O_{49}$ but gCN. For gCN and Ag(1%)–gCN, the $r(NH_4^+)$ is only 0.36 and 0.57 mg L^{-1} h^{-1} g_{cat}^{-1} respectively, as mentioned in Table 1. The $r(NH_4^+)$ over heterojunction catalyst increases obviously with increasing the $W_{18}O_{49}$ content. Ag(1%)–gCN/$W_{18}O_{49}$(1 : 1) exhibits the highest $r(NH_4^+)$, 3.2 mg L^{-1} h^{-1} g_{cat}^{-1}, which is 8.9-fold higher than that of neat gCN. According to the characterization results, this promoted N_2 photofixation ability is attributed to the improved separation rate of electron–hole pairs and enhanced light absorption in the whole solar region. Ag(1%)–gCN/$W_{18}O_{49}$(1 : 2) shows the $r(NH_4^+)$ of 2.1 mg L^{-1} h^{-1} g_{cat}^{-1}, lower than Ag(1%)–gCN/$W_{18}O_{49}$(1 : 1). This is probably due to the following two reasons. On the one hand, the content of active component Ag(1%)–gCN is too low in Ag(1%)–gCN/$W_{18}O_{49}$(1 : 2). On the other hand, Ag(1%)–gCN and $W_{18}O_{49}$ show almost the same S_{BET}. When the mass ratio Ag(1%)–gCN to $W_{18}O_{49}$ is 1 : 1, they can contact with each other as much as possible, leading to the formation of the maximum area of the heterojunction. Thus Ag(1%)–gCN/$W_{18}O_{49}$(1 : 2) shows the lower $r(NH_4^+)$ than that of Ag(1%)–gCN/$W_{18}O_{49}$(1 : 1). In addition, the $r(NH_4^+)$ over Ag(1%)–gCN/$W_{18}O_{49}$(1 : 1) remained stable over 40 h (Fig. 6b), hinting that the sample has excellent catalytic stability. Fig. 6c and d provide a preliminary analysis of the mechanism of this nitrogen photofixation process. As an electron scavenger, the addition of $KBrO_3$ sharply suppresses the nitrogen photofixation ability of Ag(1%)–gCN/$W_{18}O_{49}$(1 : 1) (Fig. 6c). The $r(NH_4^+)$ becomes very low when using DMF and DMSO (aprotic solvent) instead of water (Fig. 6d). These two results show that electrons are the reactive species and that water provides protons for this nitrogen reduction reaction. The reaction is shown in eqn (1):

$$N_2 + 6H^+ + 6e^- \rightarrow 2NH_3\uparrow \quad (1)$$

Fig. 6e shows the XPS of fresh and reused Ag(1%)–gCN/$W_{18}O_{49}$(1 : 1) in the region of W 4f. Obviously, no binding energy shift occurs after reaction indicating the stable structure of as-prepared catalysts. Fig. 6f compares the N_2 photofixation ability of Ag(1%)–gCN, Ag(1%)–gCN/$W_{18}O_{49}$(1 : 1) and other noble metal loaded gCN catalysts prepared according to previous work.[14] Obviously, the N_2 photofixation abilities of Pt(1%)-gCN, Pd(1%)–gCN and Ru(1%)–gCN are much higher than Ag(1%)–gCN, but lower than Ag(1%)–gCN/$W_{18}O_{49}$(1 : 1) under simulated solar light. This is due to the promoted separation rate and light utilization.

In order to investigate the reaction mechanism of as-prepared heterojunction catalyst, the photocatalytic RhB degradation rates over as-prepared catalysts with and without hydroxyl radical scavenger *t*-BuOH are shown in Fig. 7.[53] A 300 W Xe lamp was used as light source. It is reported that the conduction band (CB) and valence band (VB) of g-C_3N_4 are −1.12 V and +1.57 V, respectively.[43] Whereas, the redox potential for $^{\bullet}OH/OH^-$ is determined to be +1.99 V.[54] Without *t*-BuOH, the RhB degradation rates are 72%, 45% and 92% for Ag(1%)–gCN, $W_{18}O_{49}$ and Ag(1%)–gCN/$W_{18}O_{49}$(1 : 1). When *t*-BuOH is added, the RhB degradation rate for Ag(1%)–gCN shows almost no change. This indicates the addition of *t*-BuOH to trap $^{\bullet}OH$ does not influence the RhB degradation rate over Ag(1%)–gCN. This is reasonable because the VB holes in Ag(1%)–gCN are not positive enough to generate $^{\bullet}OH$. Whereas, $W_{18}O_{49}$ displays almost no activity when *t*-BuOH is added. This hints that $^{\bullet}OH$ is the only active species for RhB degradation over $W_{18}O_{49}$. It is

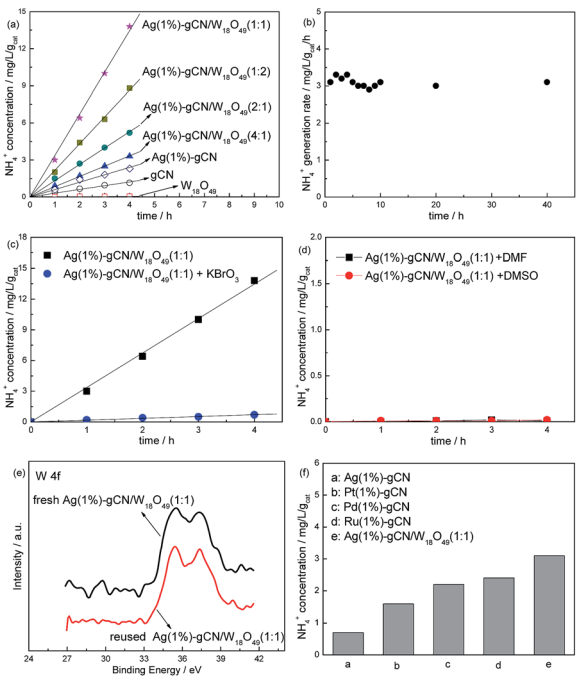

Fig. 6 Photocatalytic NH_4^+ production ability of as-prepared catalysts (a), N_2 photofixation stability of Ag(1%)–gCN/$W_{18}O_{49}$(1 : 1) (b), NH_4^+ production ability of Ag(1%)–gCN/$W_{18}O_{49}$(1 : 1) using $KBrO_3$ as the electron scavenger (c) or in aprotic solvents DMF and DMSO (d), XPS results of fresh and reused Ag(1%)–gCN/$W_{18}O_{49}$(1 : 1) in the region of W 4f (e) and N_2 photofixation ability of Ag(1%)–gCN, Ag(1%)–gCN/$W_{18}O_{49}$(1 : 1), Pt(1%)–gCN, Pd(1%)–gCN and Ru(1%)–gCN under simulated solar light (f).

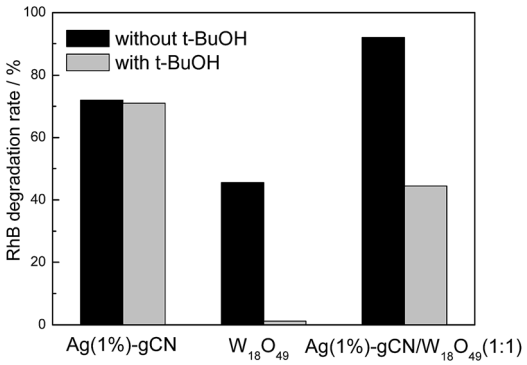

Fig. 7 Photocatalytic RhB degradation rate over as-prepared catalysts with and without *t*-BuOH.

known that the CB and VB are located at +0.74 and + 3.44 V for $W_{18}O_{49}$. The redox potential for $O_2/{}^{\bullet}O_2^-$ is −0.33 V.[54] Thus the VB holes in $W_{18}O_{49}$ are positive enough to generate ˙OH but the CB electrons are not negative enough to reduce O_2 to form ${}^{\bullet}O_2^-$. In the case of Ag(1%)–gCN/$W_{18}O_{49}$(1 : 1), the RhB degradation rate decreases sharply when *t*-BuOH is added. However, still 42% RhB is degraded indicating that ˙OH is one of the active species for RhB degradation over Ag(1%)–gCN/$W_{18}O_{49}$(1 : 1). In general, there are two typical working mechanisms for heterojunction catalyst: double charge transfer mechanism and Z-scheme mechanism.[55–58] If Ag(1%)–gCN/$W_{18}O_{49}$(1 : 1) follows the double charge transfer mechanism, the electrons and holes should be congregated at CB of $W_{18}O_{49}$ and VB of gCN. According to the energy level position, the addition of *t*-BuOH should not influence the RhB degradation rate. However, the experimental results are just the opposite. Thus, the Z-scheme mechanism over Ag(1%)–gCN/$W_{18}O_{49}$(1 : 1) is proposed (Fig. 8). Under irradiation, the photogenerated electron–hole pairs are formed in both components. Because of the abundant oxygen vacancies, there are many defect levels in the band gap of $W_{18}O_{49}$. Thus the light with long wavelength can be absorbed by $W_{18}O_{49}$, causing the photogenerated electrons continuous transition from valence band (VB) to conduction band (CB) by using these defect levels as springboard. The electrons in the CB of $W_{18}O_{49}$ combine with the holes in the VB of g-C_3N_4 at the interface of the heterojunction, leading to the enhanced electron–hole separation rate for g-C_3N_4. The CB electrons in the g-C_3N_4 transfer to the metallic Ag where the nitrogen molecules are reduced.

In order to investigate the effect of NIR light on the N_2 photofixation ability, the reaction was carried out under different light source (Fig. 9). The result indicates that neat $W_{18}O_{49}$ show no activity under each light source, confirming it is not the active component in the heterojunction catalyst. For Ag(1%)–gCN, N_2 photofixation can not occur under IR light due to no light absorption in this region. The N_2 photofixation ability of Ag(1%)–gCN under Xe lamp is almost the same as that under combined light source. Without any doubt, Ag(1%)–gCN/$W_{18}O_{49}$(1 : 1) and Ag(1%)–gCN/WO_3(1 : 1) show no N_2 photofixation ability under IR light. Under Xe lamp, the $r(NH_4^+)$ over Ag(1%)–gCN/$W_{18}O_{49}$(1 : 1) is 1.1 mg L^{-1} h^{-1} $g_{cat}{}^{-1}$, much lower

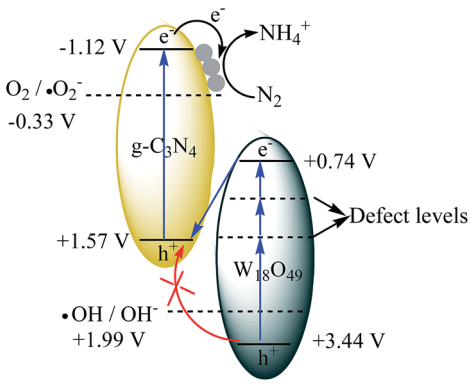

Fig. 8 The possible Z-scheme mechanism over Ag(1%)–gCN/$W_{18}O_{49}$(1 : 1).

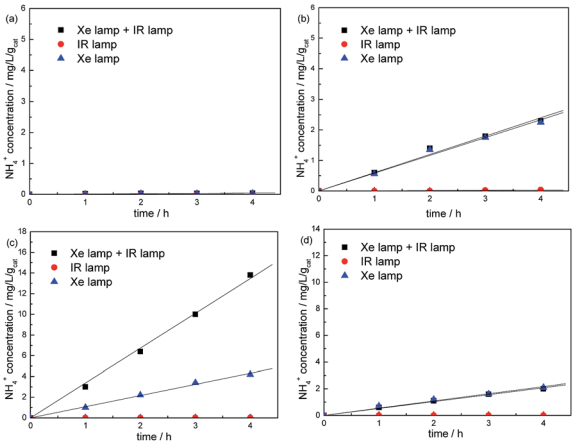

Fig. 9 Comparison of N_2 photofixation ability over $W_{18}O_{49}$ (a), Ag(1%)–gCN (b), Ag(1%)–gCN/$W_{18}O_{49}$(1 : 1) (c) and Ag(1%)–gCN/WO_3(1 : 1) (d) under different light source.

than that under combined light source (3.2 mg L^{-1} h^{-1} $g_{cat}{}^{-1}$). Whereas, the $r(NH_4^+)$ over Ag(1%)–gCN/WO_3(1 : 1) under Xe lamp is almost the same as that under combined light source (0.55 mg L^{-1} h^{-1} $g_{cat}{}^{-1}$). This value is much lower than Ag(1%)–gCN/$W_{18}O_{49}$(1 : 1) under combined light source. This confirms the crucial effect of NIR light on the N_2 photofixation performance in this reaction system. Because of the strong absorption in the full-spectrum, more photons can be utilized to produce more electron–hole pairs over $W_{18}O_{49}$. According to the Z-scheme mechanism, more photogenerated electrons can cross the heterojunction interface to combine with the holes in the VB of g-C_3N_4. Thus, the separation rate and N_2 photofixation ability are promoted.

Conclusions

In this work, full-spectrum-absorption heterojunction catalyst Ag–g-C_3N_4/$W_{18}O_{49}$ is prepared and used for N_2 photofixation under simulated solar irradiation for the first time. g-C_3N_4 is the active component in the heterojunction catalyst for N_2 reduction. $W_{18}O_{49}$ plays a role as light absorber in the full-spectrum to form more photogenerated electrons for recombining the holes in the g-C_3N_4 through "Z-scheme" mechanism. Ag(1%)–gCN/$W_{18}O_{49}$(1 : 1) exhibits the highest $r(NH_4^+)$, 3.2 mg L^{-1} h^{-1} $g_{cat}{}^{-1}$, which is 8.9-fold higher than that of neat g-C_3N_4. This is due to the improved separation rate of electron–hole pairs after coupling with $W_{18}O_{49}$ and Ag loading. Ag(1%)–gCN/$W_{18}O_{49}$(1 : 1) also displays excellent photocatalytic stability.

Conflicts of interest

There are no conflicts to declare.

Acknowledgements

This project was supported by the National Natural Science Foundation of China (51374053).

Notes and references

1 X. Chen, S. Shen, L. Guo and S. Mao, *Chem. Rev.*, 2010, **110**, 6503–6570.
2 A. Kudo and Y. Miseki, *Chem. Rev.*, 2009, **38**, 253–278.
3 M. Osterloh, *Chem. Mater.*, 2008, **20**, 35–54.
4 M. Fox and M. Dulay, *Chem. Rev.*, 1993, **93**, 341–357.
5 C. S. Guo, S. Yin, Q. Dong and T. Sato, *Nanoscale*, 2012, **4**, 3394–3398.
6 M. Yan, G. L. Li, C. S. Guo, W. Guo, D. D. Ding, S. H. Zhang and S. Q. Liu, *Nanoscale*, 2016, **8**, 17828–17835.
7 J. Tian, Y. Sang, G. Yu, H. Jiang, X. Mu and H. Liu, *Adv. Mater.*, 2013, **25**, 5075–5080.
8 G. Wang, B. Huang, X. Ma, Z. Wang, X. Qin, X. Zhang, Y. Dai and M. H. Whangbo, *Angew. Chem., Int. Ed.*, 2013, **52**, 4810–4813.
9 G. L. Li, C. S. Guo, M. Yan and S. Q. Liu, *Appl. Catal., B*, 2016, **183**, 138–142.
10 Z. Zhang and W. Wang, *Dalton Trans.*, 2013, **42**, 12072–12074.
11 Z. Z. Lou and C. Xue, *CrystEngComm*, 2016, **18**, 8406–8410.
12 X. T. Chang, S. B. Sun, L. H. Dong and Y. S. Yin, *Mater. Lett.*, 2012, **83**, 133–135.
13 G. N. Schrauzcr and T. D. Guth, *J. Am. Chem. Soc.*, 1977, **99**, 7189–7193.
14 K. T. Ranjit, T. K. Varadarajan and B. Viswanathan, *J. Photochem. Photobiol., A*, 1996, **96**, 181–185.
15 O. Rusina, O. Linnik, A. Eremenko and H. Kisch, *Chem.–Eur. J.*, 2003, **9**, 561–565.
16 G. H. Dong, W. K. Ho and C. Y. Wang, *J. Mater. Chem. A.*, 2015, **3**, 23435–23441.
17 H. Li, J. Shang, Z. H. Ai and L. Z. Zhang, *J. Am. Chem. Soc.*, 2015, **137**, 6393–6399.
18 S. Z. Hu, X. Chen, Q. Li, Y. F. Zhao and W. Mao, *Catal. Sci. Technol.*, 2016, **6**, 5884–5890.
19 S. Z. Hu, L. Ma, J. G. You, F. Y. Li, Z. P. Fan, G. Lu, D. Liu and J. Z. Gui, *Appl. Surf. Sci.*, 2014, **311**, 164–171.
20 X. C. Wang, K. Maeda, A. Thomas, K. Takanabe, G. Xin, J. M. Carlsson, K. Domen and M. Antonietti, *Nat. Mater.*, 2009, **8**, 76–80.
21 Q. F. Deng, L. Liu, X. Z. Lin, G. H. Du, Y. P. Liu and Z. Y. Yuan, *Chem. Eng. J.*, 2012, **203**, 63–70.
22 S. Z. Hu, X. Chen, Q. Li, F. Y. Li, Z. P. Fan, H. Wang, Y. J. Wang, B. H. Zheng and G. Wu, *Appl. Catal., B*, 2017, **201**, 58–69.
23 M. B. Ansari, H. L. Jin, M. N. Parvin and S. E. Park, *Catal. Today*, 2012, **185**, 211–216.
24 X. J. Bai, R. L. Zong, C. X. Li, D. Liu, Y. F. Liu and Y. F. Zhu, *Appl. Catal., B*, 2014, **147**, 82–91.
25 S. Krejcíková, L. Matejová, K. Kocí, L. Obalová, Z. Matej, L. Capek and O. Solcová, *Appl. Catal., B*, 2012, **111–112**, 119–125.
26 H. Eskandarloo, A. Badiei, M. A. Behnajady and G. M. Ziarani, *RSC Adv.*, 2014, **4**, 28587–28596.
27 J. Cao, B. D. Luo, H. L. Lin, B. Y. Xu and S. F. Chen, *Appl. Catal., B*, 2012, **111–112**, 288–296.
28 C. H. Wang, X. T. Zhang, B. Yuan, Y. X. Wang, P. P. Sun, D. Wang, Y. G. Wei and Y. C. Liu, *Chem. Eng. J.*, 2014, **237**, 29–37.
29 J. Su, L. Guo, N. Bao and C. A. Grimes, *Nano Lett.*, 2011, **11**, 1928–1933.
30 H. J. Yan, X. J. Zhang, S. Q. Zhou, X. H. Xie, Y. L. Luo and Y. H. Yu, *J. Alloys Compd.*, 2011, **509**, L232–L235.
31 L. Y. Huang, H. Xu, Y. P. Li, H. M. Li, X. N. Cheng, J. X. Xia, Y. G. Xu and G. B. Cai, *Dalton Trans.*, 2013, **42**, 8606–8616.
32 X. C. Wang, K. Maeda, X. F. Chen, K. Takanabe and K. Domen, *J. Am. Chem. Soc.*, 2009, **131**, 1680.
33 S. J. Liu, F. T. Li, Y. L. Li, Y. J. Hao, X. J. Wang, B. Li and R. H. Liu, *Appl. Catal., B*, 2017, **212**, 115–128.
34 F. T. Li, Y. Zhao, Q. Wang, X. J. Wang, Y. J. Hao, R. H. Liu and D. S. Zhao, *J. Hazard. Mater.*, 2015, **283**, 371–381.
35 K. N. Song, F. Xiao, L. J. Zhang, F. Yue, X. Y. Liang, J. D. Wang and X. T. Su, *J. Mol. Catal. A: Chem.*, 2016, **418–419**, 95–102.
36 X. X. Guo, X. Y. Qin, Z. J. Xue, C. B. Zhang, X. H. Sun, J. B. Hou and T. Wang, *RSC Adv.*, 2016, **6**, 48537–48542.
37 P. Q. Chen, M. L. Qin, Y. Liu, B. R. Jia, Z. Q. Cao, Q. Wan and X. H. Qu, *New J. Chem.*, 2015, **39**, 1196–1201.
38 M. Guan, C. Xiao, J. Zhang, S. Fan, R. An, Q. Cheng, J. Xie, M. Zhou, B. Ye and Y. Xie, *J. Am. Chem. Soc.*, 2013, **135**, 10411–10417.
39 W. Bi, C. Ye, C. Xiao, W. Tong, X. Zhang, W. Shao and Y. Xie, *Small*, 2014, **10**, 2820–2825.
40 C. S. Guo, S. Yin, M. Yan, M. Kobayashi, M. Kakihana and T. Sato, *Inorg. Chem.*, 2012, **51**, 4763–4771.
41 W. R. Zhao, J. Zhang, X. Zhu, M. Zhang, J. Tang, M. Tan and Y. Wang, *Appl. Catal., B*, 2014, **144**, 468–477.
42 G. Xi, S. Ouyang, P. Li, J. Ye, Q. Ma, N. Su, H. Bai and C. Wang, *Angew. Chem., Int. Ed.*, 2012, **51**, 2395–2399.
43 Y. Wang, X. C. Wang and M. Antonietti, *Angew. Chem., Int. Ed.*, 2012, **51**, 68–89.
44 P. Wang, B. B. Huang, X. Y. Qin, X. Y. Zhang, Y. Dai, J. Y. Wei and M. H. Whangbo, *Angew. Chem., Int. Ed.*, 2008, **47**, 7931–7933.
45 L. Ge and C. Han, *Appl. Catal., B*, 2012, **117–118**, 268–274.
46 W. Lei, D. Portehault, R. Dimova and M. Antoniettit, *J. Am. Chem. Soc.*, 2011, **133**, 7121–7127.
47 Y. W. Zhang, J. H. Liu, G. Wu and W. Chen, *Nanoscale*, 2012, **4**, 5300–5303.
48 Y. S. Fu, T. Huang, L. L. Zhang, J. W. Zhu and X. Wang, *Nanoscale*, 2015, **7**, 13723–13733.
49 R. Wu, J. Zhang, Y. Shi, D. Liu and B. Zhang, *J. Am. Chem. Soc.*, 2015, **137**, 6983–6986.
50 B. L. He, B. Dong and H. L. Li, *Electrochem. Commun.*, 2007, **9**, 425–430.
51 D. Wang, J. B. Sun, X. Cao, Y. H. Zhu, Q. X. Wang, G. C. Wang, Y. Han, G. Y. Lu, G. S. Pang and S. H. Feng, *J. Mater. Chem. A.*, 2013, **1**, 8653–8657.
52 V. N. Khabashesku, J. L. Zimmerman and J. L. Margrave, *Chem. Mater.*, 2000, **12**, 3264–3270.
53 S. Q. Zhang, Y. X. Yang, Y. N. Guo, W. Guo, M. Wang, Y. H. Guo and M. X. Huo, *J. Hazard. Mater.*, 2013, **261**, 235–245.

54 G. Liu, P. Niu, L. C. Yin and H. M. Cheng, *J. Am. Chem. Soc.*, 2012, **134**, 9070–9073.
55 K. Kondo, N. Murakami, C. Ye, T. Tsubota and T. Ohno, *Appl. Catal., B*, 2013, **142–143**, 362–367.
56 Y. M. He, L. H. Zhang, B. T. Teng and M. H. Fan, *Environ. Sci. Technol.*, 2015, **49**, 649–656.
57 Y. M. He, L. H. Zhang, X. X. Wang, Y. Wu, H. J. Lin, L. H. Zhao, W. Z. Weng, H. L. Wan and M. H. Fan, *RSC Adv.*, 2014, **4**, 13610–13619.
58 Y. M. He, L. H. Zhang, M. H. Fan, X. X. Wang, M. L. Walbridge, Q. Y. Nong, Y. Wu and L. H. Zhao, *Sol. Energy Mater. Sol. Cells*, 2015, **137**, 175–184.